Study of anisotropic character induced by microscale laser shock peening on a single crystal aluminum

Hongqiang Chen, Youneng Wang,[a] Jeffrey W. Kysar, and Y. Lawrence Yao
Department of Mechanical Engineering, Columbia University, New York, New York 10027

(Received 31 July 2006; accepted 16 November 2006; published online 18 January 2007)

The beam spot size used in microscale laser shock peening is of the same order as grain size in many materials. Therefore, the deformation is induced in only a few grains so that it is necessary to treat the material as being anisotropic and heterogeneous. In order to investigate the corresponding anisotropic features, different experimental techniques and three-dimensional finite element simulations are employed to characterize and analyze anisotropic responses for single crystal aluminum under single pulse shock peening at individual locations. X-ray microdiffraction techniques based on a synchrotron light source affords micron scale spatial resolution and is used to measure the residual stress spatial distribution along different crystalline directions on the shocked surface. Crystal lattice rotation due to plastic deformation is also measured with electron backscatter diffraction. The result is experimentally quantified and compared with the simulation result obtained from finite element analysis. The influence of crystalline orientation is investigated using single crystal plasticity in finite element analysis. The results of the finite element simulations of a single shock peened indentation are compared with the finite element results for a shocked line of plain strain deformation assumption. The prediction of overall characters of the anisotropic characters associated with microscale laser shock peening will lay the ground work for the practical application of microscale laser shock peening. © *2007 American Institute of Physics*.
[DOI: 10.1063/1.2424500]

I. INTRODUCTION

Laser shock peening (LSP) is a well-established technique which is used to introduce a compressive residual stress state into the near surface region of a treated material.[1,2] An ablative material which can be as simple as spray paint or black adhesive tape is applied to the surface to be laser shock peened and the specimen is then immerged in a liquid, typically water. A high intensive laser with energy densities of the order of several GW/cm^2 is then directed at the ablative surface with a very short pulse time on the order of tens of nanoseconds. Much of the laser fluence is absorbed by the ablative material so that the ablative material is vaporized into a plasma.[3] The surrounding liquid confines the resulting pressure wave so that a shock wave propagates into the material, which induces plastic deformation into the near surface region. The resulting residual stress state near the surface is compressive, which has been shown to enhance the fatigue life of treated components.[1]

Most of the previous implementations of laser shock peening have employed lasers with a spot size of several millimeters.[1,4] Recently, however, this technique has been extended to the microscale by focusing the laser to a spot size of about 10 μm (Refs. 2 and 5) and then applying a raster of laser shock peens over the region to be treated. The technique has been shown to enhance the fatigue life of the target.[5] Microscale laser shock peening has the advantage of being able to use a much less expensive and smaller laser than with larger laser spots. In addition the process can be applied to highly localized regions of stress concentration, and also the technique can be used on small and even micro-sized components.

One issue which arises in the case of microscale laser shock peening (μLSP) is that the grain size of a typical material being treated may be approximately the same as the laser spot size. Therefore, induced plastic deformation will occur predominately in only a few grains of the material so that the material must be treated as being anisotropic and heterogeneous, rather than isotropic and homogeneous. For that reason the actual residual stress state attained from the process will depend upon the details of the structure and orientation of the grains affected by μLSP so that the residual stress states induced in the near surface will lie within a range of possible values.

In an effort to determine the range of possible residual stress states, μLSP is applied to a single crystal in the present study to characterize the effect of material anisotropy without the complicating factor of heterogeneity. The goal of this paper then is to experimentally characterize the residual stress state of the crystal after the application of μLSP which will act as a base line for numerical simulations of the process. Future studies will concentrate on laser shock peening near the grain boundary of a bicrystal. Ultimately, numerical simulations, which have been validated against both sets of experiments, will be employed to predict the range of possible residual stress states induced by μLSP while accounting for many different realizations of grain size and orientation which might be encountered in a treated material.

The experimental techniques used in this study are capable of micron scale spatial resolution. Atomic force mi-

[a]Electronic mail: yw2119@columbia.edu

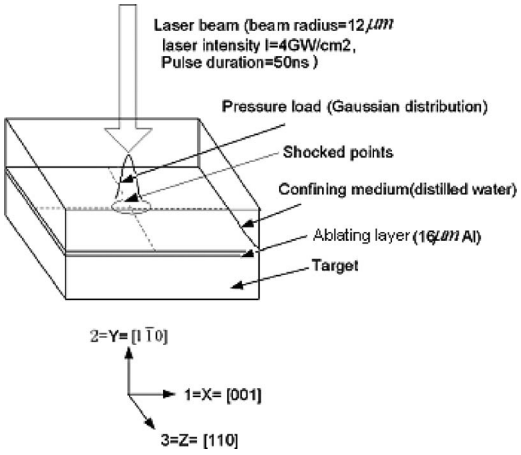

FIG. 1. Sample geometry and shock peening condition of single crystal Al (110).

croscopy (AFM) is used to determine the profile of the shocked surface, electron backscatter diffraction (EBSD) is used to measure the crystal lattice rotation which accompanies the plastic deformation, and x-ray microdiffraction techniques are used to spatially resolve information about the residual stress state. The finite element method is employed in this study to perform the numerical simulations. The main goal of the simulation is to investigate the effect of anisotropy on the residual deformation and stress state. Therefore, the process is modeled as quasistatic; fully dynamic simulations will be employed in future studies.

This paper is organized as follows. The specimen preparation and laser shock process conditions are detailed in Sec. II. The experimental characterization is discussed in Sec. III. The simulations are presented in Sec. IV. Conclusions are presented in Sec. V.

II. EXPERIMENTAL CONDITIONS

Fully annealed single crystals of pure aluminum (grown by the seeded Bridgman technique) were used in the experiments. The crystallographic orientation was identified by Laue x-ray diffraction and the sample was cut to shape, as shown in Fig. 1, using a wire electrical discharge machining (EDM). The coordinate system used throughout this paper is indicated in Fig. 1 and defined as follows: x axis is parallel to [001] direction, y axis is parallel to $[1\bar{1}0]$ direction, and z axis is parallel to the crystal direction of [110]. In preparation for laser shock peening, the $(1\bar{1}0)$ surface of the sample was polished mechanically by using grit 600 sandpaper and then repeated by using grit 1200 sandpaper. The specimen was then polished using diamond paste with lapping oil as lubricant, first 6 μm paste and then 1 μm with minimum pressure until no preferred scratches were apparent. In order to remove any residual deformation induced during the mechanical polish process, the sample was electropolished before shocking. The electrolyte contains 30% volume nitric acid (ACS purity, concentration of 67%) and 70% volume methyl alcohol. The sample was electropolished at 10.0 V for 30 s at −20 °C. The sample and aluminum alloy are anode and cathode, respectively. Figure 2(a) shows an AFM scan of the surface prior to laser shock peening, and Fig. 2(b) shows a cross section; the surface roughness is about 50.1 nm. The ablative material was then attached to the $(1\bar{1}0)$ surface. The first step was to apply a thin layer (~10 μm) of high vacuum grease made by Dow Corning Corporation (Midland, MI) to minimize heat conduction from the coating to the target, followed by the application of a 16 μm thick polycrystalline aluminum foil, chosen for its relatively low threshold of vaporization.[5] The sample was placed in a shallow container filled with distilled water about 3 mm above the sample's top surface to confine the pressure generated during the peening process. The laser fluence used to perform the shock peening had a wavelength of $\lambda = 355$ nm and was generated using a frequency tripled Q-switched Nd:YAG (yttrium aluminum garnet) laser in TEM_{00}, the simplest transverse electromagnetic mode.[6] The diameter of the laser spot was 12 μm and it had a radial Gaussian energy distribution, measured by the knife-edge method.[6] A single laser pulse of duration of 50 ns with pulse energy of 228 μJ, measured via a standard power meter [PE10 of Ophir Optronics, Inc. (Wilmington, MA)], yielded an average laser intensity of 4.03 GW/cm^2. The aluminum foil was ablated, and the resulting shock wave generated a "dentlike" shocked region and the $(1\bar{1}0)$ surface.

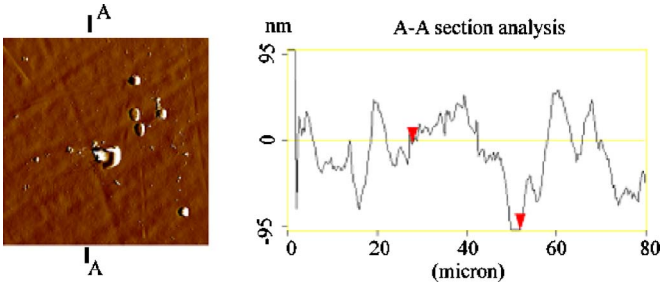

FIG. 2. (Color online) Typical surface profile of unshocked surface and shocked region from AFM. (a) Top view of unshocked sample surface. (b) Cross section of unshocked surface.

III. POSTPEENING MATERIAL CHARACTERIZATION

A. Deformation geometry measured by AFM

The geometry of the shocked region was determined by means of atomic force microscopy in noncontact mode (Dimension 3000 of Digital Instruments Nanoscope Inc.). A typical surface profile of the shocked region is in Fig. 3(a); the scan area is 100×100 μm^2. The depth of the shocked region is around 2.0 μm with diameter close to 80 μm. The deformed profiles along a line which runs through the approximate center of the shocked region parallel to the [001] direction and along a similar line parallel to the [110] in Fig. 3(a) are shown in Fig. 3(b). It should be noted that the spatial range of the AFM was insufficient to measure the profiles in Fig. 3(b) in one measurement; therefore the profiles in Fig. 3(b) are composite profiles from several measurements. It can be seen that the general trend of the profile along different directions is the same; however, the lateral extent in [001] is slightly larger than that in the [110] direction. The asymmetry of the deformation is evidently caused by the anisotropic nature of the single crystal, because the intensity

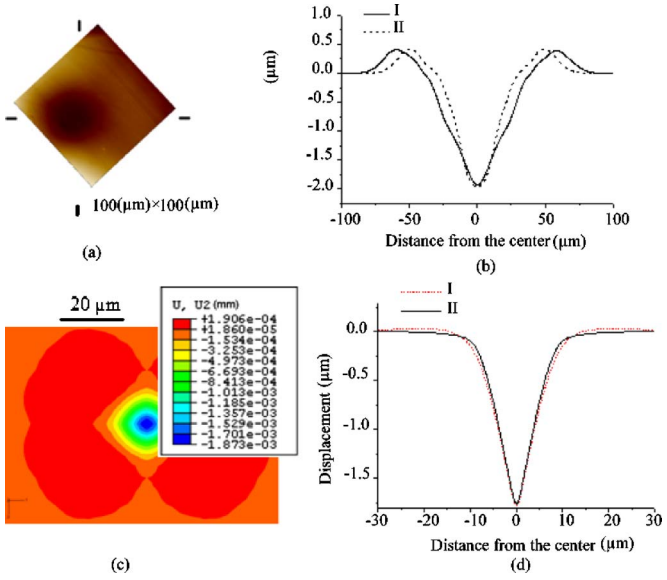

FIG. 3. (Color online) Typical surface profile of shocked region. (a) Top view of shocked region from AFM. (b) Cross sections of shock region from AFM. (c) Depth deformation contour (150×150 μm^2) by FEM. (d) Depth distribution along lines I and II.

distribution of the laser is axisymmetric. Pileup exists around the shock peen due to the approximate incompressible behavior of the material as it is plastically deformed.

B. X-ray microdiffraction measurement

1. X-ray microdiffraction measurement scheme

The x-ray facilities of the synchrotron radiation source (beamline X20A) at the National Synchrotron Light Source (NSLS) at Brookhaven National Lab were used in this study. The x-ray beam at this facility can be focused by a tapered glass capillary to spot sizes as small as 3 μm which allows the characterization of the residual stress state to be made with micron-scale resolution. In addition the extreme intensities allow a short sampling time. Complete details of the x-ray microdiffraction measurement can be found elsewhere.[5]

A schematic of the x-ray diffraction setup is shown in Fig. 4(a). The Bragg condition for a given set of lattice planes can be achieved only when the normal to the lattice planes bisects and is thus contained within the geometrical plane of the incident and the diffracted x-ray beams. The diffractometer employed is a commercial Huber two-circle vertical instrument equipped with partial theta (θ) and chi (χ) arcs. Assuming that the incident beam shape is a smooth, well-defined function, such as a Gaussian, the mean beam vector will be the most intense ray. Consequently, it is ensured that the mean beam vector, and not any other, satisfies the Bragg condition by rotating the specimen using the θ and χ scan adjustments until the maximum intensity is located in the detector.[7] Once the specimen tilt is properly set, the 2θ value of the peak can be measured by a detector scan in 2θ or by a radial scan where 2θ and θ are stepped at the symmetric 2:1 ratio. The *x*-*y*-*z* stage onto which the diffractometer is mounted is used to move the specimen so that the x-ray diffraction measurements can be made over a grid of points as shown in Fig. 4(b).

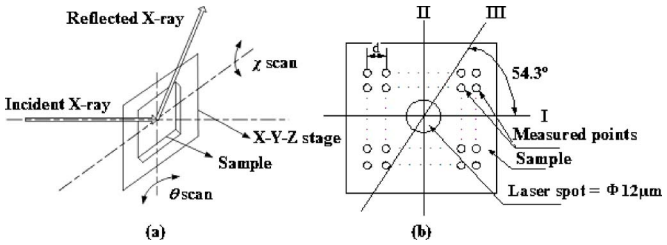

FIG. 4. (a) θ and χ scans of sample/stage. (b) X-ray microdiffraction measurement scheme (I: [001] direction, II: [110] direction, and III: [111] direction).

For face-centered cubic metals, the diffraction structure factor for (110) is zero and the reflections are absent,[8] so the (220) reflections are chosen for x-ray diffraction measurement. In order to spatially resolve the residual stress induced by μLSP, measurements were made in a grid pattern over the shocked region as shown in Fig. 4(b). The spacing between adjacent measurement points is 5 μm when within 20 μm of the shock center and is 10 μm at distances greater than 20 μm from the shock center. At each position, the corresponding x-ray diffraction profile was recorded. The shape of the profile and its shift can be interpreted in terms of the residual stress state, as will be discussed in the next section.

For the Al $(1\bar{1}0)$ surface in Fig. 1, the crystalline structure has special directions along lines denoted as I, II, and III which correspond, respectively, to [001], [110], and [111] directions. In order to study the anisotropic behavior of single crystals which undergo μLSP, the x-ray diffraction profiles along those directions were investigated, in addition to making measurements over the grid.

2. Diffraction profile analysis

Subprofile analysis using the composite model by Ungar *et al.*[9] was employed to interpret the diffraction profiles. A short summary of the model follows. It is assumed that a dislocation cell structure which consists of "cell interiors" and "cell wall" exists in the plastically deformed metal. The cell walls parallel to the compressive axis are under a residual compressive stress $\Delta\sigma_w<0$, and the cell interiors are under a tensile stress $\Delta\sigma_c>0$. The asymmetric Bragg reflections can then be separated into the sum of two symmetric peaks which correspond to cell interiors and cell wall. For brevity, the subscripts *w* and *c* will be used to indicate walls and cell interiors, respectively. The asymmetric line profiles I are assumed to be composed of two components I_w and I_c, where I_w is attributed to the cell-wall material and I_c to the cell-interior material. The centers of both components are shifted in opposite directions in accordance with $\Delta\sigma_w = E(\Delta d/d)|_w<0$ and $\Delta\sigma_c = E(\Delta d/d)|_c>0$, where E is Young's modulus and d is the spacing between atomic planes. We introduce a Cartesian coordinate system with the z axis parallel to the normal direction and the x and y axes perpendicular to the two sets of walls. Then, a measure of the residual stresses can be characterized by the absolute value of the difference $\sigma_{zz}=\pm|\Delta\sigma_w-\Delta\sigma_c|$, and the sign is negative if the main subprofile peak is at the left side, and vice versa.

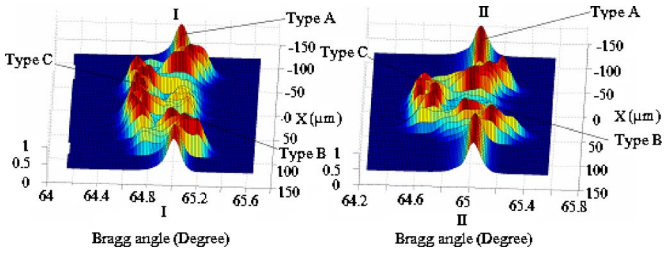

FIG. 5. (Color online) Typical x-ray diffraction profile spatial distribution along lines I [001] and II [110].

Their range of influence is of the order of the cell dimensions which is longer than the range of individual dislocations in a random distribution, e.g., in cell walls or in cell interiors. The lateral residual stress in the sample surface plane is then estimated as $\sigma_{xx}=\sigma_{yy}=-\sigma_{zz}\nu$, where ν denotes Poisson's ratio.

Figure 5 shows the typical three-dimensional spatial distribution of the measured x-ray diffraction intensity profiles of the (220) Bragg reflection along line I ([001] direction). The salient features of these line profiles can be summarized as follows:

(a) When the measure point moved across the shock center from left to right along line I in Fig. 5, the line profiles change distinctively from a single symmetric peak to asymmetry with a second peak becoming visible and finally return to a single symmetric peak. It is clear that after shock peening, the x-ray profile was significantly broadened and became asymmetric compared to the unshocked region.

(b) At ±100 μm and beyond, the measured profile peak value is almost at the theoretical angle, which in turn represents the shock-free regions. This type of diffraction profile will be referred to as type A, herein. As the shock is approached, the main peak shifts towards larger diffraction angles, while a second peak pops up toward a smaller diffraction angle (type B diffraction profile); for the region near the shock center, the main peak shifts towards smaller diffraction angles, while a second peak pops up toward a larger diffraction angle (type C diffraction profile).

The type B profiles indicate a tensile residual lateral stress state because the Bragg angle increases, which indicates a decrease of the lattice spacing of the $(2\bar{2}0)$ planes parallel to the sample surface. Since after shock peening this surface has zero traction, the decrease in lattice spacing corresponds to the Poisson contraction of a lateral residual tensile stress state. Conversely, type C profiles indicate a compressive residual stress state since the Bragg angle decreases.[5] The striking transition from type C to type B away from the shock region indicates a fundamental change in the residual stress state independent of subprofile interpretation. The x-ray diffraction profiles show similar patterns along different crystalline directions (line I and line II). However, for the broadened asymmetric profile, the type C profile is more significant along line I [001] than line II [110], while the type B profile is dominant along line II. The area with broadened and shifted profiles is smallest along line II [110], followed by line III [111] and line I [001].

The interpretation of diffraction profiles in highly deformed regions is often ambiguous. Nevertheless it should be emphasized that qualitative differences of the diffraction profiles as a function of position relative to the shocked region strongly suggest a transition from compressive to tensile residual stress state, independent of the specific methods used to interpret the diffraction profiles quantitatively.

3. Approximate residual stress distribution from x-ray measurement

After obtaining the x-ray diffraction profile at different positions in the shocked region, the resulting spatial distribution of the estimated stress across the shocked region is plotted in Fig. 6(a). The stress can be considered to be an average stress in the region sampled by x-ray diffraction. A compressive residual stress is generated near the center of the shocked region bordered by a region of tensile stress. Although the laser spot size is only 12 μm, the high shock pressure in μLSP can generate significant compressive residual stresses over a much larger region. The compressive stress is estimated to have a maximum value of −120 MPa near the center and cover an ellipselike region which extends ±60 μm along [001] direction and ±25 μm along [110] direction from the center. The maximum residual tensile stress is estimated to be +90 MPa and occurs in [110] direction approximately 40 μm away from the shock center, while the minimum residual tensile stress exists in [001] direction. In order to study the influence of crystal direction on residual stress distribution, Fig. 7 shows the estimated lateral residual stress distribution on the Al (110) sample surface along [001], [111], and [110] directions. The distributions show similar patterns for different directions. Compressive residual stress exists in the shocked dent center, and tensile stress exists at the outer range of dent. Again, the compressive residual stress extends further in [001] than [110].

C. EBSD measurement of lattice rotation

EBSD is a diffraction technique for obtaining crystallographic orientation with submicron spatial resolution from bulk samples or thin films in a scanning electron microscope (SEM). EBSD was employed in previous work[10] to investigate crystal lattice rotation caused by plastic deformation during high-strain rate laser shock peening in single crystal aluminum and copper samples of $(1\bar{1}0)$ and (001) orientations to enable the measurement of the in-plane lattice rotation under approximate plane strain conditions. For the single dent shock peening, lattice rotation on the shocked surface is measured to give insight into the three-dimensional (3D) plastic deformation and anisotropic properties of a single crystal under μLSP. The accuracy of crystallographic orientation obtained via EBSD measurements is about 0.5°.

1. EBSD measurement scheme

EBSD measurements were performed on the sample surface over a region $(150\times150\ \mu m^2)$ which is larger than the

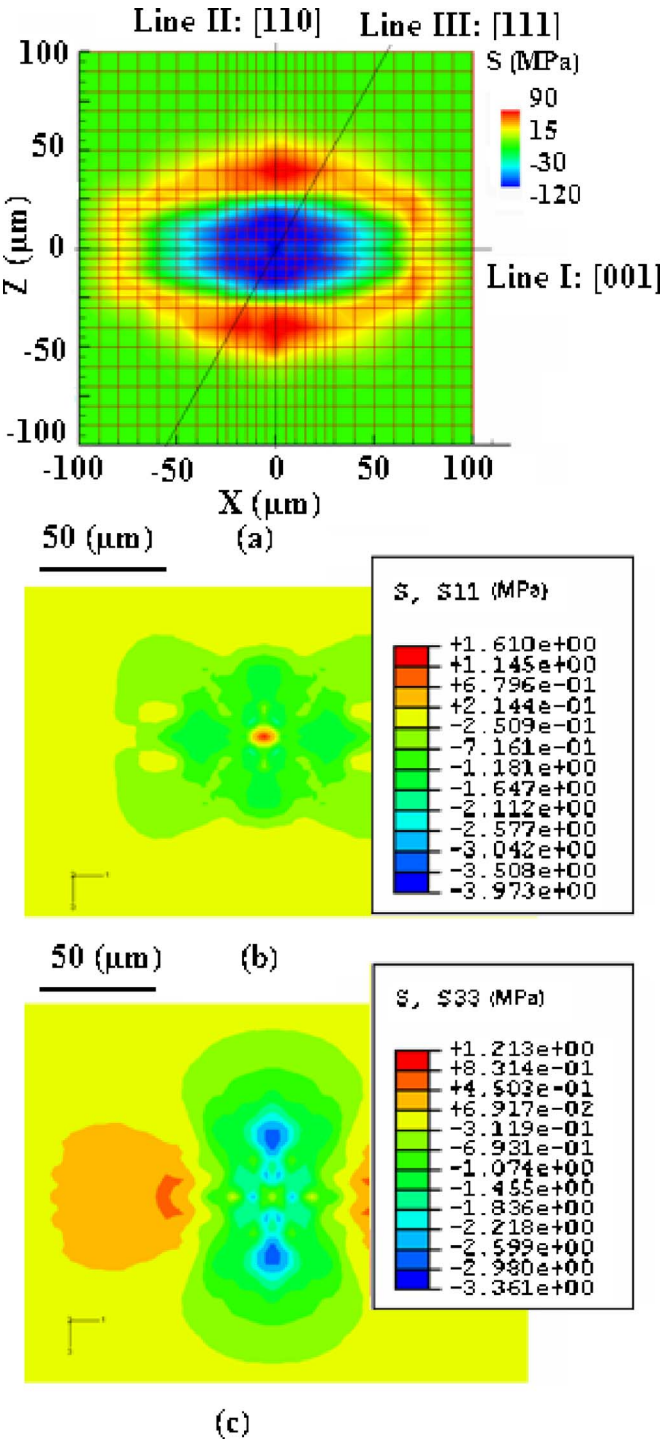

FIG. 6. (Color online) Surface residual stress distribution contour (a) from x-ray microdiffraction, (b) in 11 direction of FEM simulation, and (c) in 33 direction of FEM simulation.

shock peen. The EBSD data were collected using a system supplied by HKL Technology and attached to a JEOL JSM 5600LV scanning electron microscope. All data were acquired in the automatic mode, using external beam scanning and employing a 1 μm step size. The EBSD results from each individual measurement comprise data containing the position coordinates of the electron beam as well as the three Euler angles, which collectively describe the orientation of the particular interaction volume relative to the orientation of the specimen in the SEM. This information allows the in-

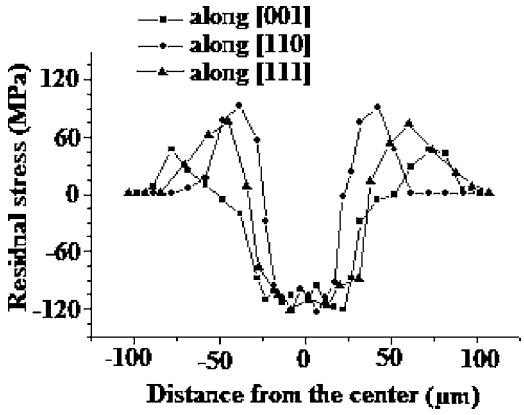

FIG. 7. (Color online) Lateral residual stress distribution from x-ray diffraction measurement for Al (110) sample.

plane and the out-of-plane lattice rotations to be calculated relative to the known undeformed crystallographic orientation, which serves as the reference state.

2. Lattice rotation field from EBSD

As discussed in Chen *et al.*,[10] the crystalline orientation will change after laser shock peening due to plastic deformation. Figure 8 illustrates contours of out-of-plane lattice rotations obtained from EBSD, which describes the orientation difference of the $[1\bar{1}0]$ lattice direction before and after μLSP for the shocked region on Al $(1\bar{1}0)$ sample top surface $(150\times150\ \mu m^2)$. The lattice rotation is measured as the angle between the $[1\bar{1}0]$ lattice direction in the undeformed state and in the deformed state. The green region of Fig. 8 corresponds to the shock-free region since there is no change from the original crystal orientation. The red region indicates a lattice rotation of up to 5°. It is not surprising that the contour distribution is approximately twofold symmetric axis about the *Y* axis. The maximum misorientation occurs about 10 μm away from the center, and the overall region with significant orientation change is ellipselike with major axis about 80 μm along the [001] direction and minor axis about 50 μm along the [110] direction. The overall shape is consistent with the surface profile as measured by AFM mea-

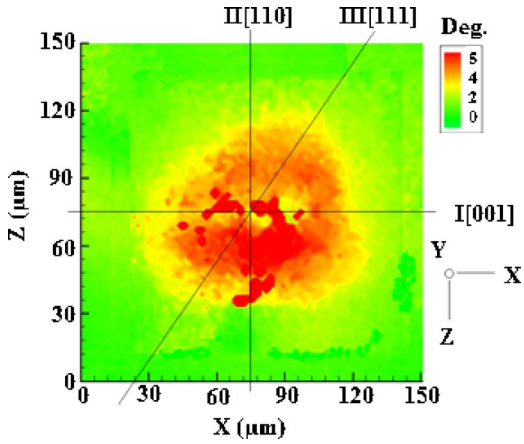

FIG. 8. (Color online) Crystal misorientation angle distribution on sample surface by EBSD measurement.

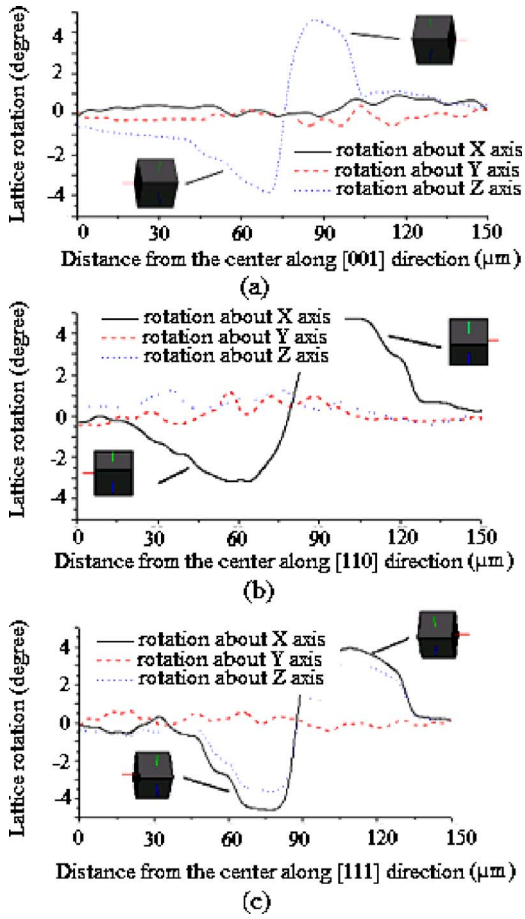

FIG. 9. (Color online) Crystalline orientation change on sample surface; lattice rotation is magnified by a factor of 3 for viewing clarity.

surement in Figs. 3(a) and 3(b). Thus, the misorientation contour indicates the affected region of plastic deformation in μLSP. As a control, EBSD measurements were made on an unshocked surface and all measurements of orientation were within ±0.5°.

Figures 9(a)–9(c) shows the lattice rotation around X, Y, and Z axes separately for Al (110) sample from EBSD measurement. In order to study the anisotropic characteristics, the lattice rotation distributions along three typical crystal directions, [001], [110], and [111], on the $(1\bar{1}0)$ surface are compared. In [001] direction, the lattice rotation around the Z axis is ±4° between ±40 μm from the center of the shocked region and the rotation direction is approximately antisymmetric on both sides of the shock center. The rotations about the other axes are negligibly small. The lattice rotation about the X axis along the [110] direction is approximately ±4° antisymmetric on both sides of the shocked center, with an extent of about ±60 μm from the center of the shocked region which is larger than that in [001] direction. In [111] direction, rotations about both X and Z axes are observed and the antisymmetric value is ±4° between ±50 μm from the center of the shocked region. For rotation about the Y axis (surface normal), the value is almost zero along all three directions which indicates that the lattice rotation around surface normal is very small after μLSP.

IV. FEM SIMULATIONS

A. Simulation conditions

In this section, finite element (FEM) analyses were carried out to analyze the response of single crystal aluminum under μLSP. Instead of assuming a two-dimensional deformation state, the material deformation is considered as a full three-dimensional problem. A user-material subroutine (UMAT) for single crystal plasticity written by Huang[11] and modified by Kysar[12] and based on the theory of Asaro[13] is incorporated into the finite element analysis using the general purpose finite element program ABAQUS/STANDARD. The simulation is a two-step quasistatic loading and unloading process corresponding to the shock peening and relaxation processes. The computation domain is $300\times300\times300$ μm^3; element C3D8RH and bias mesh are used with minimum mesh size of 1.2 μm in the center. In the simulation, X (11), Y (22), and Z (33) coordinates in Fig. 1 are chosen as [001], [110], and $[1\bar{1}0]$ directions, respectively. The loading conditions are as follows. On top surface (XZ plane), a spatially nonuniform shock pressure with a Gaussian spatial distribution is applied as

$$P(x,z) = P_0 \exp\left(-\frac{x^2+z^2}{2R^2}\right), \tag{1}$$

where x and z is the distance from the center of the laser beam along X and Z directions. P_0 is the peak value of shock pressure and the plasma radius $R=10$ μm here.[2] The peak value of pressure is assumed to be $P_0/\tau_{\mathrm{CRSS}}=13$. As for boundary conditions of the three-dimensional model, the applied surface tractions correspond to the applied pressure on the shocked surface. At the bottom surface, the vertical displacement is specified to be zero and the outer edges are traction free. In the simulation, elastic-ideally plastic behavior is assumed so that hardening is neglected. The simulation ignores rate and inertial effects but does include the effects of finite lattice rotations.

B. Deformation geometry measured from FEM simulation

Figure 3(c) shows the deformation depth distribution on the shocked surface predicted by FEM simulation. The red region corresponds approximately to the material pileup which is positive, and the blue region corresponds to the maximum depth of the shocked region. It is clear that the deformation is not axisymmetric due to the anisotropy of the single crystal. Figure 3(d) shows the predicted surface profile along lines I and II. The distribution is similar to the AFM measurements in Fig. 3(b), except that the width of the predicted shock region is narrow. Thus, the typical deformation geometry under μLSP is not a circular but an ellipselike dent. Deformation extends farther along [001] direction than [110] direction.

In order to study the plastic anisotropic character in detail, the Schmid factor of each active slip systems is investigated. Suppose the loading direction is l, the slip plane normal is n, and the slip direction is s, the Schmid factor can be represented as $\cos\phi\cos\lambda=(n\cdot l)(s\cdot l)$, where ϕ is the angle

TABLE I. Schmidt factor for each slip system for loading direction $[1\bar{1}0]$.

Slip plane n	Slip direction s	Schmidt factor for loading direction $l=[1\bar{1}0]$
(111)	$[\bar{1}10]$	0
	$[10\bar{1}]$	0
	$[0\bar{1}1]$	0
$(\bar{1}11)$	$[110]$	0
	$[101]$	$-1/\sqrt{6}$
	$[0\bar{1}1]$	$-1/\sqrt{6}$
$(1\bar{1}1)$	$[110]$	0
	$[10\bar{1}]$	$1/\sqrt{6}$
	$[011]$	$-1/\sqrt{6}$
$(11\bar{1})$	$[\bar{1}10]$	0
	$[101]$	0
	$[011]$	0

between n and l and λ is the angle between s and l. The twelve slip systems in Fcc Al are shown in Table I and the loading direction is $[1\bar{1}0]$ as seen in Fig. 1.

As seen in Table I, for uniaxial loading along $[1\bar{1}0]$ direction, four of the twelve slip systems will be activated simultaneously since the magnitudes of the Schmid factors are the same. As is well known, six active slip systems are necessary to specify an arbitrary strain state. The assumption of constant volume for plastic strain requires that the trace of the plastic strain tensor be zero. As a consequence, there are only five independent components of plastic strain so that five active slip systems are needed to achieve any arbitrary ε_{ij}^{p}. Since only four slip systems are activated in the present case, an arbitrary deformation state cannot be attained. Rice[14] showed that the four slip systems under question can combine to form two effective slip systems which act in the (110) plane when they are activated in equal amounts. An arbitrary deformation state within that plane can be achieved because under plane strain condition there are only two independent plastic strain components and three effective slip systems. Thus, shock loading generates a predominately plane deformation state in (110) plane, which is parallel to the direction of line I [001]. Therefore, plastic deformation along [001] direction (line I) is much easier than that in the [110] direction (line II), which accounts for the ellipselike structure of the shocked region.

C. Approximate residual stress distribution from simulation

Through FEM simulation, the distribution of residual stress induced by μLSP can be studied and compared with the x-ray measurement results. Figures 6(b) and 6(c) show the residual stress distribution on the sample surface. It is clear that the magnitude and sign of residual stresses σ_{11} and σ_{33} are similar and most regions are covered by the compressive residual stress. In the subprofile analysis of x-ray diffraction profile, it is assumed that a biaxial stress state exists in the sample surface, so that the calculated lateral residual stress is an approximation for σ_{11} and σ_{33}.

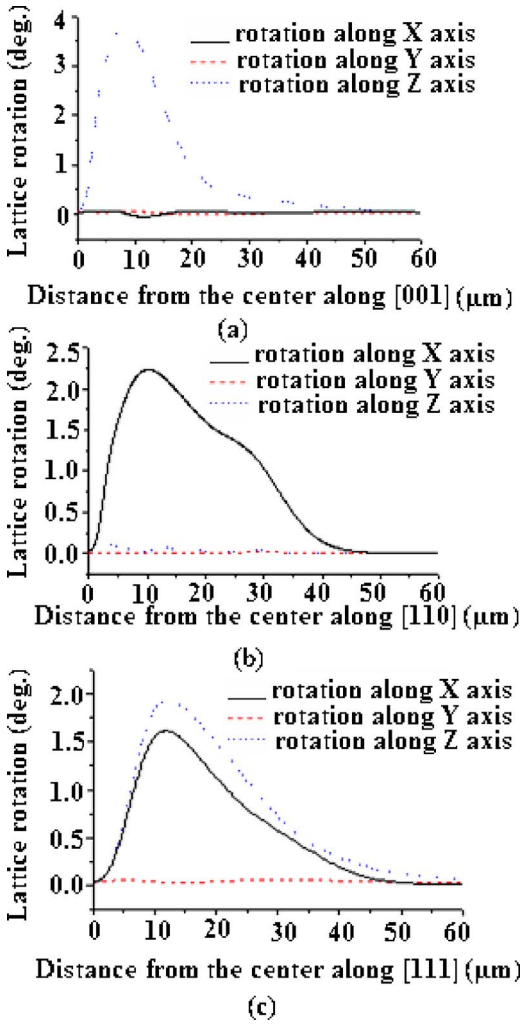

FIG. 10. (Color online) Lattice rotation along the three axes on Al (110) sample surface.

Comparing the results of FEM simulation and x-ray measurement, it can be seen that both show the same overall trend for residual stress distribution along different directions which is caused by the anisotropic characteristic of single crystal. It is found from the experiment that the compressive residual stress extends further in the [001] direction than [111] and [110] directions, which may help develop strategies to optimize the μLSP process by applying shocks at greater distances along the $\langle 001 \rangle$ than along $\langle 111 \rangle$ and $\langle 110 \rangle$.

D. Lattice rotation field from simulation

Through FEM analysis of material response under μLSP with single crystal plasticity, the lattice rotation distribution can be simulated and compared with the EBSD measurement result. Figures 10(a)–10(c) show the lattice rotation about the X, Y, and Z axes along different directions ([001], [110], and [111]) on sample surface. The pattern is similar with there in Figs. 9(a)–9(c) except that only half region is shown here. From the simulation, it is clear that the lattice rotation is mainly around X and Z axes while very small around Y axis

which is the surface normal. These results are consistent with the EBSD measurement in Fig. 8(a). The lattice rotation close to the center of the shocked region is near zero, and the rotation increases to a maximum value, then decreases on a radial line from the center of the shocked region. The significant lattice rotation ($>1°$) occurs at 5–30 μm in [110] direction and 5–20 μm in [001] direction. The affected region along [111] direction is between the other two directions, which is from 10 to 25 μm. Thus, the lattice rotation is not axisymmetric about the shock center which is caused by the anisotropic characteristic of single crystal.

V. CONCLUSIONS

3D plastic deformation induced by microscale laser shock peening on single crystal aluminum (110) surface was investigated with x-ray microdiffraction, EBSD, AFM, and 3D FEM simulation based on single crystal plasticity. The laser beam size is 12 μm with intensity at 4 GW/cm^2. AFM measurements show that the plastic deformation region is larger in [001] direction (±60 μm) along [001] direction than the [110] direction (±25 μm) with depth around 2 μm, which is consistent with the FEM result. The spatial distribution of residual stress state in the shocked region was measured by x-ray microdiffraction, and a compressive residual stress estimated to be as large as −120 MPa was found in an ellipselike indentation region 50×80 μm^2 near the center. Tensile stress was estimated to be up to +90 MPa near the outer edge of indentation. The plastic deformation and compressive residual stress extends further along [001] direction while the tensile stress is more confined in [110] direction. 3D FEM simulations show similar residual stress distribution as x-ray measurement. EBSD measurement and 3D FEM simulation both show that the lattice rotation is around 3° up to 50 μm away from the shock center. The lattice rotation distribution along different crystal directions makes it possible to estimate the length-scale dependence of the plastic deformation.

The experimental methodology and results presented herein enable a systematic study of the micro scale laser shock peening process. It is now possible to systematically measure and simulate the extent and character of three dimensional plastic deformation, residual stresses and crystal lattice rotation fields with micron spatial resolution. Thus, the anisotropic plastic behavior of the single crystal under μLSP can be studied and these simulations will lay the ground work for more realistic simulations, which account for rate effects, hardening, and a dynamic loading.

ACKNOWLEDGMENTS

This work was supported by the National Science Foundation under Grant No. NSF DMI-02-00334 and AFOSR FA5550-06-1-0214. Guidance in x-ray microdiffraction provided by Dr. I. Cev Noyan and Dr. Jean Jordan-Sweet is appreciated.

[1] A. H. Clauer and J. H. Holbrook, *Shock Waves and High Strain Phenomena in Metals-Concepts and Applications* (Plenum, New York, 1981), p. 675.
[2] W. Zhang and Y. L. Yao, ASME J. Manuf. Sci. Eng. **124**, 369 (2000).
[3] J. A. Fox, Appl. Phys. Lett. **24**, 461 (1974).
[4] P. Peyre, R. Fabbro, P. Merrien, and H. P. Lieurade, Mater. Sci. Eng., A **A210**, 102 (1996).
[5] H. Chen, J. W. Kysar, and Y. L. Yao, ASME Trans. J. Appl. Mech. **71**, 713 (2004).
[6] W. M. Steen, *Laser Material Processing*, 2nd ed. (Spring-Verlag, London, 1994).
[7] I. C. Noyan, P.-C. Wang, S. K. Kaldor, and J. L. Jordan-Sweet, Rev. Sci. Instrum. **71**, 1991 (2000).
[8] B. D. Cullity, *Elements of X-ray Diffraction*, 2nd ed. (Addison-Wesley, London, 1978), pp. 13–20.
[9] T. Ungar, H. Mughrabe, D. Ronnpagel, and M. Wilkens, Acta Metall. **32**, 333 (1984).
[10] H. Chen, J. W. Kysar, and Y. L. Yao, ASME Trans. J. Appl. Mech. **71**, 713 (2004).
[11] Y. Huang, Division of Applied Sciences, Harvard University, Mech Report No. 178, 1991 (unpublished).
[12] J. W. Kysar, Division of Engineering and Applied Sciences, Harvard University, Addendum to Mech Report No. 178, 1997 (unpublished).
[13] R. J. Asaro, Adv. Appl. Mech. **23**, 1 (1983).
[14] J. R. Rice, Mech. Mater. **6**, 317 (1987).